PHYSICAL REVIEW D **94,** 024023 (2016)

How loud are neutron star mergers?

Sebastiano Bernuzzi,[1,2] David Radice,[2] Christian D. Ott,[3,2] Luke F. Roberts,[2] Philipp Mösta,[4,2] and Filippo Galeazzi[5]

[1]*DiFeST, University of Parma, and INFN, I-43124 Parma, Italy*
[2]*TAPIR, Walter Burke Institute for Theoretical Physics, California Institute of Technology, 1200 E California Boulevard, Pasadena, California 91125, USA*
[3]*Yukawa Institute for Theoretical Physics, Kyoto University, Kitashirakawa-Oiwakecho, Sakyo-Ku, Kyoto 606-8502, Japan*
[4]*Department of Astronomy, University of California at Berkeley, 501 Campbell Hall 3411, Berkeley, California 94720, USA*
[5]*Institut für Theoretische Physik, Max-von-Laue-Straße 1, 60438 Frankfurt, Germany*

(Received 23 December 2015; published 11 July 2016)

We present results from the first large parameter study of neutron star mergers using fully general relativistic simulations with finite-temperature microphysical equations of state and neutrino cooling. We consider equal and unequal-mass binaries drawn from the galactic population and simulate each binary with three different equations of state. Our focus is on the emission of energy and angular momentum in gravitational waves in the postmerger phase. We find that the emitted gravitational-wave energy in the first ∼10 ms of the life of the resulting hypermassive neutron star (HMNS) is about twice the energy emitted over the entire inspiral history of the binary. The total radiated energy per binary mass is comparable to or larger than that of nonspinning black hole inspiral-mergers. About 0.8–2.5% of the binary mass-energy is emitted at kHz frequencies in the early HMNS evolution. We find a clear dependence of the postmerger gravitational wave emission on binary configuration and equation of state and show that it can be encoded as a broad function of the binary tidal coupling constant κ_2^T. Our results also demonstrate that the dimensionless spin of black holes resulting from subsequent HMNS collapse are limited to $\lesssim$0.7–0.8. This may significantly impact the neutrino pair annihilation mechanism for powering short gamma-ray bursts (sGRB).

DOI: 10.1103/PhysRevD.94.024023

I. INTRODUCTION

Gravitational wave (GW) astronomy has been inaugurated by the first direct detection of GWs from a binary black hole (BH) merger by Advanced LIGO [1]. Another primary source for Advanced LIGO is the GW-driven inspiral and merger of binary neutron stars (BNS). A possible outcome of the merger is the formation of a hot, differentially rotating hypermassive neutron star (HMNS), which may survive for many tens of milliseconds before collapsing to a BH, e.g. [2–6]. Observations of NSs with mass $\sim 2M_\odot$ [7,8] and of BNSs with individual masses $\sim 1.35M_\odot$ [9] favor the HMNS scenario as the initial outcome. The stiff nuclear equation of state (EOS) in combination with differential rotation at least temporarily prevents collapse to a BH [10]. GW emission is expected to depend on the interplay of several physical ingredients: relativistic (magneto)hydrodynamics (M)HD, nonlinear gravity, finite-temperature effects in the nuclear EOS, neutrino cooling, and angular momentum redistribution [via viscosity or (M)HD]. Fully general relativistic (GR) simulations that include realistic microphysics (i.e. nuclear and neutrino physics) are the only reliable means to study postmerger evolution and its GW emission.

In this work, we present results from a new and largest-to-date set of BNS configurations simulated in full numerical relativity with temperature-dependent microphysical EOS and neutrino physics. Our configurations are representative of galactic BNS systems. We consider three different EOS broadly consistent with observational and experimental constraints. We focus on the postmerger evolution and its GW emission, and show for the first time that the HMNS phase is the most GW-luminous phase in the entire history of BNS systems. Soft EOS and HMNS masses close to (but below) the prompt collapse threshold are the most luminous. BHs resulting from HMNSs that survive for $\gtrsim$10 ms are robustly limited to dimensionless spins $\lesssim$0.7. Larger spins are obtained if the merger remnant collapses promptly or within 1–2 dynamical times of merger.

II. BINARY CONFIGURATIONS AND SIMULATIONS

The properties of the considered binary configurations are summarized in Table I. We choose equal and unequal-mass configurations guided by observed galactic BNS systems [9]. Configurations *-135135, *-136125, *-140120, and *-144139 reproduce the NS masses in the binaries identified by B2127 + 11C (and B1534 + 12), J1906 + 0746, J1756-2251 (and J1829 + 2456), and B1913 + 13, respectively. We simulate these binaries using three different nuclear EOS, referred to as LS220 [11], DD2 [12], and SFHo [13]. They span a reasonable

TABLE I. BNS properties (EOS, individual isolation masses, total baryonic mass of the binary, ADM quantities, dimensionless tidal coupling constant, e.g. [16]) and the dimensionless radiated GW energy per binary mass $E_{\rm GW}/M$ and the mass-rescaled angular momentum J/M^2 at t_0 (merger) and t_N (N ms after merger). For configurations collapsing to a BH we also report $E^c_{\rm GW}/M$ and J^c/M^2 as computed $\sim$1 ms after collapse and the BH irreducibile mass and dimensionless angular momentum as measured by the horizon finder. All numbers are from simulations with $\Delta x = 295$ m. The total binary mass is $M = M_A + M_B$. Configurations are named according to EOS and masses M_A,M_B.

							$E_{\rm GW}(t)/M \times 10^2$				$J(t)/M^2 \times 10^1$							
EOS	M_A $[M_\odot]$	M_B $[M_\odot]$	M_b $[M_\odot]$	$M_{\rm ADM}$ $[M_\odot]$	$J_{\rm ADM}$ $[GM_\odot^2/c]$	κ_2^T	t_0	t_{10}	t_{20}	t_{50}	t_0	t_{10}	t_{20}	t_{50}	$E^c_{\rm GW}/M$ $\times 10^2$	J^c/M^2 $\times 10^1$	$M_{\rm BH}$ $[M_\odot]$	$a_{\rm BH}$ $\times 10^1$
DD2	1.40	1.20	2.829	2.576	6.537	203	1.27	2.13	2.17	2.18	8.87	7.95	7.90	7.89	···	···	···	···
DD2	1.365	1.25	2.843	2.589	6.639	194	1.34	2.24	2.29	2.31	8.87	7.91	7.86	7.83	···	···	···	···
DD2	1.35	1.35	2.946	2.673	7.015	162	1.37	2.56	2.58	2.60	8.75	7.57	7.54	7.53	···	···	···	···
DD2	1.44	1.39	3.100	2.799	7.589	124	1.46	2.90	2.95	2.97	8.60	7.29	7.25	7.23	···	···	···	···
LS220	1.40	1.20	2.830	2.574	6.540	159	1.34	2.09	2.31	2.35	8.79	8.03	7.81	7.78	···	···	···	···
LS220	1.365	1.25	2.846	2.588	6.623	151	1.38	2.89	3.05	3.12	8.76	7.35	7.20	7.15	···	···	···	···
LS220	1.35	1.35	2.947	2.671	7.000	125	1.46	3.32	3.63	···	8.65	7.0	6.81	···	3.80	6.68	2.40	5.44
LS220	1.44	1.39	3.102	2.797	7.570	94	1.52	···	···	···	8.51	···	···	···	3.68	6.92	2.70	7.04
SFHo	1.40	1.20	2.850	2.573	6.525	115	1.53	3.21	3.37	3.48	8.47	7.06	6.92	6.84	···	···	···	···
SFHo	1.365	1.25	2.868	2.589	6.615	110	1.52	3.61	3.80	3.94	8.47	6.78	6.63	6.53	···	···	···	···
SFHo	1.35	1.35	2.972	2.674	7.018	89	1.59	···	···	···	8.38	···	···	···	3.77	6.86	2.56	6.83
SFHo	1.44	1.39	3.133	2.801	7.581	67	1.66	···	···	···	8.26	···	···	···	2.27	7.86	2.79	8.08

range of radii and maximum gravitational masses for nonspinning NSs: DD2 has $M^{\rm TOV}_{\rm max} \sim 2.42 M_\odot$ and radius $R_{1.35M_\odot} \sim 13.2$ km; SFHo and LS220 have similar $M^{\rm TOV}_{\rm max} \sim 2.05 M_\odot$, but $R_{1.35M_\odot} \sim 11.9$ km (SFHo) and $R_{1.35M_\odot} \sim 12.7$ km (LS220). We refer to EOS with larger $R_{1.35M_\odot}$ as being "stiffer," since at fixed mass, a stiffer EOS results in lower central densities and larger NS radii. All three EOS provide maximum cold NS masses greater than $2M_\odot$, which puts them in agreement with the maximum observed NS mass [7,8]. SFHo and LS220 fall within the NS mass radius relation predicted by [14], while DD2 has a somewhat larger radius. SFHo and DD2 both agree with microscopic neutron matter calculations [15], but LS220 falls outside of the favored region.

We compute conformally-flat initial data for our simulations, assuming quasicircular orbits and irrotational flow [17]. They are characterized by the Arnowitt-Deser-Misner (ADM) mass-energy $M_{\rm ADM}$ and angular momentum $J_{\rm ADM}$. The initial separation is 40 km ($\sim$3 orbits to merger). The spacetime is evolved with the Z4c formulation [18], coupled with GRHD and a neutrino leakage scheme [19]. We employ the EinsteinToolkit [20] with the CTGamma spacetime solver and the WhiskyTHC GRHD code [21]. We use the high-order MP5 reconstruction implemented in WhiskyTHC to ensure that the effect of numerical dissipation is minimized. The Courant-Friedrichs-Lewy factor is set to 0.15 to guarantee the positivity preserving property of the limiter described in [21]. Dynamical evolutions are carried out with linear resolution of $\Delta x = 295$ m for a total time of $\sim$60 ms after merger, and with $\Delta x = 185$ m for 20 ms after merger. Our grid consists of 6 refinement levels with the coarsest being a cube of linear extent $1024 M_\odot \simeq 1512$ km. To reduce our computational cost, we impose symmetry across the xy-plane and, for equal mass models, we assume π-symmetry. Model LS220-135135 is simulated also without leakage. The GWs are extracted from the spin-weighted multipolar decomposition of the Weyl scalar Ψ_4 on a sphere placed at $200 M_\odot \simeq 295$ km.

In all simulations but SFHo-144139, we observe the formation of a HMNS. We define the merger time t_0 as the time of waveform peak amplitude [22]; time periods of N ms after t_0 are indicated as t_N. Figure 1 shows the evolution of the maximum rest-mass density $\rho_{\rm max}(t)$ for all models and snapshots of the temperature T and rest-mass density ρ in the orbital plane at representative times for LS220-135135 (with leakage).

During merger, the two NS cores come into contact and merge to a single core within $\sim t_{10}$. $\rho_{\rm max}$ increases by up to a factor 1.5–2 and oscillates violently. Note that for a given total mass, stiffer EOS have smaller $\rho_{\rm max}$. Additionally, the oscillations in $\rho_{\rm max}$ have higher amplitude when the configuration is closer to the prompt collapse threshold and when $\rho_{\rm max}$ is larger. The evolution from the initial two-core structure into a more axisymmetric single-core HMNS is due to hydrodynamic angular momentum redistribution and dissipation by shock heating and GW emission [3]. The extreme nonaxisymmetric shape and the increase in density result in very efficient GW emission [22].

Temperatures as high as $\sim$50 MeV are reached in the interface between the NSs (Fig. 1). Physically, we expect these temperatures to be somewhat lower, because at very high resolutions and when MHD is included, [23] showed

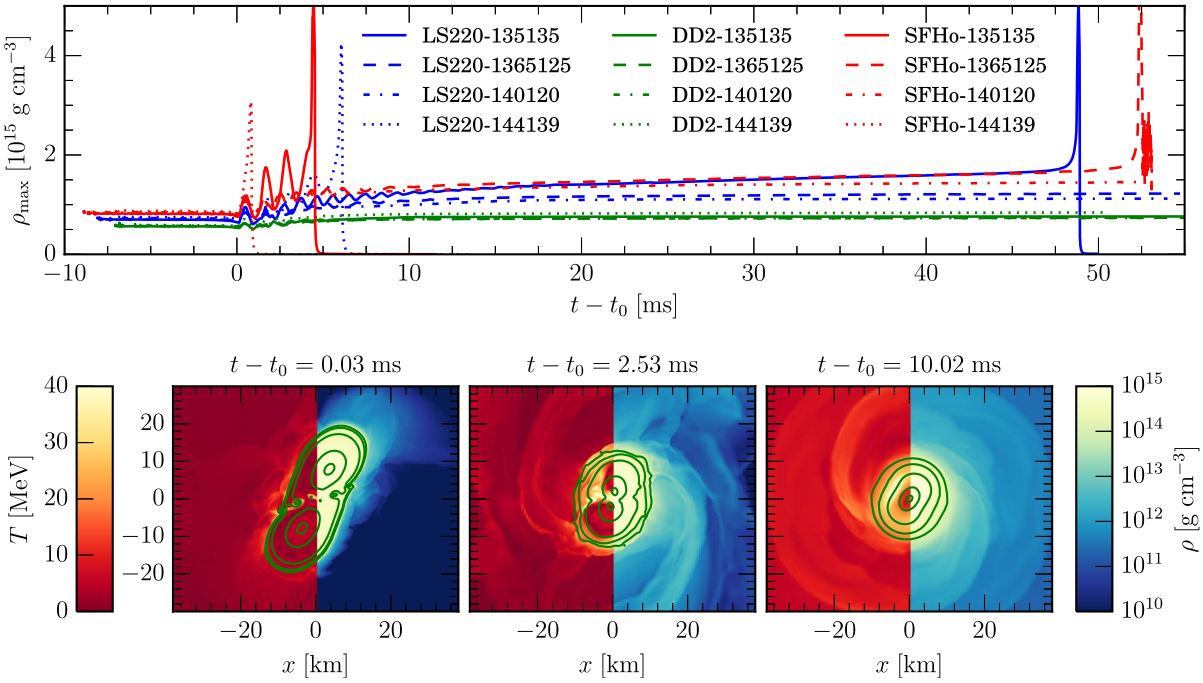

FIG. 1. Top: evolution of the maximum rest-mass density $\rho_{\rm max}$ for all the configurations. For simulations times $t < t_0$, $\rho_{\rm max}$ is the maximum value of the densest star; after contact and merger $\rho_{\rm max}$ is the absolute maximum. Bottom: color coded temperatures and density at three representative times for LS220-135135. The black contours enclose densities larger than 10,20,40,80 and 98% of $\rho_{\rm max}$. The core of the HMNS remains relatively cold, with $T \simeq 10$ MeV and is surrounded by a hot shell $T \simeq 40$ MeV of material at densities $\sim 5 \times 10^{14}$ g cm^{-3}.

that a fraction of the shear flow energy created at contact is converted into magnetic field energy. In our simulations, instead, the unresolved shear energy is converted into heat by our finite-volume scheme. This corresponds to a case in which no large-scale dynamo is activated and the locally generated magnetic field dissipates.

As the merger and the early HMNS evolution proceed, we observe hot streams of matter being squeezed out of the interface between the two NSs. Part of this material becomes unbound while the rest forms a thick torus around the merger remnant. As the two NS cores merge, the core remains relatively cold, with $T \sim 10$ MeV, while the temperature peaks at around $\sim$50 MeV at densities of ~ 3–5×10^{14} g cm^{-3}. Even at these lower densities, the EOS is only mildly affected by thermal effects [10].

The high mass of SFHo-144139, combined with the particularly soft EOS, results in prompt collapse at merger. We observe BH formation within the simulated time also for LS220-1365125, LS220-135135, LS220-144139, SFHo-135135. It is interesting to note that LS220 and SFHo have similar cold nonspinning NS maximum masses, but SFHo HMNSs collapse much more quickly. This is due to their more compact postmerger configuration, which leads to a more rapid evolution toward instability [10]. We list the remnant BH masses and spins in Table I. The properties of the accretion disks will be discussed elsewhere [24].

III. GW ENERGY

The energy radiated in GWs over the entire history of the binary up to the start of our simulations ($t = 0$), is (in $G = c = 1$) $E_{{\rm GW},i} = M - M_{\rm ADM}$, where $M = M_A + M_B$ is the binary gravitational mass at infinite separation. From the Ψ_4 projections we compute the waveform multipoles $h_{\ell m}(t)$ up to $\ell = \ell_{\rm max} = 8$, and, using Eqs. (15) and (16) of [25], the energy and angular momentum emitted in GWs during our simulations, $\Delta E_{\rm GW}(t)$ and $\Delta J_{\rm GW}(t)$, respectively. The total emitted energy over inspiral, merger, and postmerger evolution to time t is then $E_{\rm GW}(t) = E_{{\rm GW},i} + \Delta E_{\rm GW}(t)$. Similarly, the binary angular momentum to time t is given by $J(t) = J_{\rm ADM} - \Delta J_{\rm GW}(t)$. We report both quantities normalized by M at different times in Table I.

A gauge-invariant way to represent the HMNS GW emission is to consider binding energy vs. angular momentum curves in analogy to the approach proposed in [25,26]. Working with quantities per reduced mass, we define $E_b = -E_{\rm GW}/(M\nu)$ and $j = J/(M^2\nu)$ with the symmetric mass ratio $\nu = M_A M_B/M^2 \approx 1/4$. Representative examples of $E_b(j)$ curves are shown in Fig. 2. The binary evolution starts at large j (large separations) and at small negative E_b, accounting for the energy radiated over the inspiral until the point our simulations start. GW emission drives the system to smaller j and lower E_b. Importantly, the largest

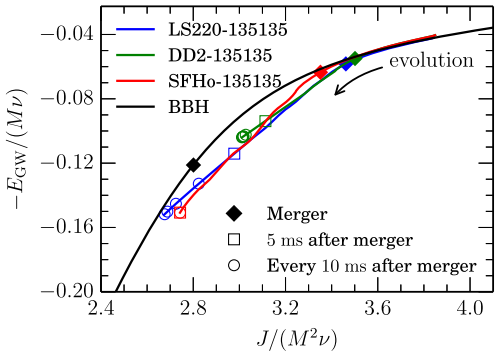

FIG. 2. BNS dynamics in terms of gauge-invariant binding energy vs. angular momnetum curves. Equal-mass configurations are compared to the corresponding nonspinning BH binary. The largest GW luminosity comes from the HMNS, and the overall energy emission (relative to the mass) from BNS is in many cases larger than the BH inspiral-merger case (excluding ringdown). These features are common to all our simulated BNS.

change of E_b and j (corresponding to the highest GW luminosity) occurs within t_{10} after merger. Furthermore, the $E_b(j)$ curves in the HMNS phase are approximately linear, indicating that the main emission is at an approximately constant frequency proportional to the derivative $\partial E_b/\partial j$ [22].

During inspiral and up to merger (t_0, diamonds in Fig. 2), the BNS typically emits 1.27–1.66% of its initial mass-energy M [16]. *The energy emission within t_{10} is up to twice as large as the energy emitted during the whole inspiral*. By the end of our simulations (t_{50} or collapse), the BNS has typically emitted ∼2.18–3.93% of M (cf. Fig. 2). This fractional energy emission is comparable to—or larger than—that of a nonspinning equal-masses BH binary inspiral-merger (∼3%), excluding the ringdown (∼5%). However, quasicircular BH binaries with aligned spins can emit up to 13% of M [27,28]; high-energy BH collisions up to ∼60% [29]. If the HMNS survives for $t > t_{20}$, then the GW energy contribution from the subsequent part of the evolution is negligible. These considerations hold also for configurations like LS220-144139, whose HMNS collapses within t_{10}, but obviously not for the prompt collapse case SFHo-144139 (no HMNS).

Our results show that the details of the above depend crucially on EOS and binary mass. In general, for fixed masses, the stiff DD2 EOS gives the smallest energy emission. For fixed EOS, the larger the total mass, the larger is the GW energy emission relative to the total mass. However, in the case of a configuration close to the collapse threshold that collapses soon after merger ($\Delta t \ll t_{10}$), lower rather than higher masses favor GW energy/angular momentum emission (cf. LS220-144139 vs. LS220-135135 and SFHo-135135 vs. SFHo-136125).

The dimensionless mass-rescaled angular momentum available at merger is in the range $3.3 \lesssim j(t_0) \lesssim 3.6$ ($0.83 \lesssim J(t_0)/M^2 \lesssim 0.89$); this range is representative of a large sample of EOS, masses, and mass ratios [16,22]. The GW emission during the early HMNS evolution reduces these values by 11–22%, depending on binary configuration and EOS. The late-time value of $J(t)/M^2$ is the largest spin $a_{\rm BH}$ that the remnant BH can have (assuming no disk is produced). For HMNSs that collapse within t_{50}, an upper limit for the BH spin parameter is $\max(a_{\rm BH}) \lesssim 0.7$ ($j \lesssim 2.8$ for $\nu = 1/4$, cf. Fig. 2). The angular momentum evolution of HMNSs that are stable beyond t_{50} is expected to be significantly affected by MHD angular momentum redistribution and breaking and is presently highly uncertain.

Runs at higher-resolution (HR) show that our results are robust and actually conservative: the GW luminosity is typically underestimated due to numerical dissipation at low resolution. The HMNS collapse time t_c can vary by a few milliseconds for configurations close to the collapse threshold, e.g. LS220-144139 has $t_c \sim t_6$ for $\Delta x = 185$ m runs, while $\sim t_{10}$ for $\Delta x = 290$ m. The respective $E_{\rm GW}(t_{20})$ variation is, at most, $\lesssim$10% at HR. However, because a HMNS that collapses earlier also emits more GWs early on, the timescale of the main GW emission remains $\sim t_{10}$.

IV. DISCUSSION

We demonstrate for the first time that, due to the extreme densities and nonaxisymmetry of the early post-merger phase, generic BNS mergers can reach large GW luminosity corresponding to $L_{\rm GW} \sim 6 \times 10^{55}$ erg s^{-1}, with typical emission timescale of $\sim t_{10}$ (compare with [1]). Our results lead us to the conjecture that the maximum postmerger GW emission efficiency is attained by a configuration in which EOS and binary mass are such that the HMNS is slightly below the prompt collapse threshold and supported for $\sim t_{10}$. Such configurations can be identified by investigating the dependence on the coupling constant for tidal interactions [22]. The latter is defined as $\kappa_2^T = \kappa_2^A + \kappa_2^B$, with $\kappa_2^A = 2k_2^A(X_A/C_A)^5 M_B/M_A$, where C_A is the compactness of star A, $X_A = M_A/M$, and k_2^A the quadrupolar dimensionless Love number [25]. Large values of κ_2^T correspond to stiff EOS (large Love numbers) and individual stars with low compactness, see Table I. The number κ_2^T parametrizes, at leading order, tidal interactions during the orbital phase and is the key parameter to effectively characterize merger dynamics and postmerger GW frequencies [22]. The total GW energy is shown as a function of κ_2^T in Fig. 3, which includes results from high- and low-resolution simulations. These results suggest that the maximum GW efficiency is obtained for binaries with $70 \lesssim \kappa_2^T \lesssim 150$. This is a narrow range compared with the ∼10–500 range of values that κ_2^T may assume for BNS systems [16]. The efficiency maximum is caused by the competition between BH formation, occurring earlier for smaller κ_2^T, and the GW energy emission decreasing with increasing κ_2^T. A larger κ_2^T corresponds to a larger tidal

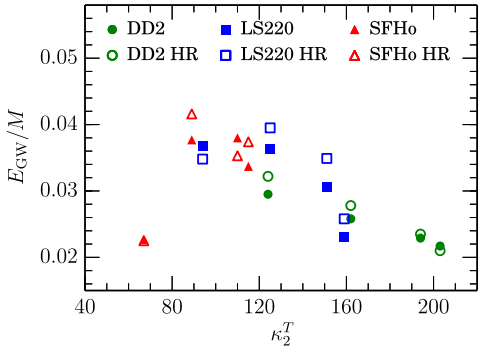

FIG. 3. Dimensionless and mass-rescaled GW energy at t_{20} (or $t_c < t_{20}$) as a function of the tidal coupling constant κ_2^T [16].

disruption radius, a less compact postmerger configuration with a smaller angular frequency, and therefore less energy loss relative to angular momentum loss.

Observational constraints on the EOS could be obtained by combining a single GW energy measurement with the results in Fig. 3. More simulations and a more accurate characterization of the relation $E_{GW}(\kappa_2^T)$ are required for this purpose. Most importantly, observing the large GW luminosities reported here will be challenging for the Advanced LIGO/Virgo detectors because of the high frequency (2–4 kHz) nature of the emission. The typical horizon distance for a signal-to-noise ratio 9 is ∼10 Mpc for an optimally oriented source. Unless optimized sensitivity curves at high-frequencies are developed, the postmerger GW spectrum will remain a target for third generation detectors [30].

Due to the short timescale of the GW emission (t_{10}), physical processes other than hydrodynamics and shock-heating are unlikely to affect the emission. For the LS220-135135 case, we have verified that neutrino cooling does not affect the GW emission in t_{50}. Similarly, MHD effects are expected to influence the GW luminosity only if they can significantly affect the short-timescale HMNS dynamics. The magnetorotational instability (MRI) and its ability to redistribute angular momentum might drive the HMNS to an early collapse. This can be characterized by an effective viscosity, which is currently poorly constrained, but simulations of [31] suggest an angular momentum redistribution timescale of $\mathcal{O}(100)$ ms. Thus, also for the MRI, we expect little influence on the GW luminosity. Future, very high-resolution MHD simulations are necessary to further test this assertion [23,31,32].

Finally, our new limit on the spin of the final BH has important consequences for models of sGRBs relying on the energy deposition by neutrino pair-annihilation. There, the energy deposition rate depends strongly on the BH spin [33]. For fixed accretion rate, the energy deposition by neutrinos from a disk accreting onto a BH with $a = 0.7$ can be up to a factor ∼100 times smaller than for a disk feeding a maximally spinning BH [33]. Our limit on a does not significantly constrain sGRB models invoking magnetic effects, which can easily account for the required energies even in absence of extremely high BH spin, e.g., [34].

ACKNOWLEDGMENTS

We thank B. S. Sathyaprakash for triggering this work. This research was partially supported by the Sherman Fairchild Foundation and by NSF under Grants No. CAREER PHY-1151197, No. PHY-1404569, and No. AST-1333520. The simulations were performed on the Caltech computer Zwicky (NSF PHY-0960291), on NSF XSEDE (TG-PHY100033), and on NSF/NCSA Blue Waters (NSF PRAC ACI-1440083). L. R. and P. M. were supported by NASA Einstein Postdoctoral Fellowships under Grants No. PF3-140114 and No. PF5-160140, respectively.

[1] B. P. Abbott *et al.* (Virgo, and LIGO Scientific Collaborations), Phys. Rev. Lett. **116**, 061102 (2016).
[2] S. Rosswog and M. B. Davies, Mon. Not. R. Astron. Soc. **345**, 1077 (2003); S. Rosswog and M. Liebendoerfer, Mon. Not. R. Astron. Soc. **342**, 673 (2003).
[3] M. Shibata and K. Taniguchi, Phys. Rev. D **73**, 064027 (2006).
[4] Y. Sekiguchi, K. Kiuchi, K. Kyutoku, and M. Shibata, Phys. Rev. Lett. **107**, 051102 (2011).
[5] A. Bauswein and H. T. Janka, Phys. Rev. Lett. **108**, 011101 (2012).
[6] K. Hotokezaka, K. Kiuchi, K. Kyutoku, T. Muranushi, Y. Sekiguchi, M. Shibata, and K. Taniguchi, Phys. Rev. D **88**, 044026 (2013); C. Palenzuela, S. L. Liebling, D. Neilsen, L. Lehner, O. L. Caballero, E. O'Connor, and M. Anderson, *ibid.* **92**, 044045 (2015).
[7] P. Demorest, T. Pennucci, S. Ransom, M. Roberts, and J. Hessels, Nature (London) **467**, 1081 (2010).
[8] J. Antoniadis *et al.*, Science **340**, 1233232 (2013).
[9] B. Kiziltan, A. Kottas, M. De Yoreo, and S. E. Thorsett, Astrophys. J. **778**, 66 (2013).
[10] J. D. Kaplan, C. D. Ott, E. P. O'Connor, K. Kiuchi, L. Roberts, and M. Duez, Astrophys. J. **790**, 19 (2014).
[11] J. M. Lattimer and F. Douglas Swesty, Nucl. Phys. **A535**, 331 (1991).
[12] S. Typel, G. Röpke, T. Klähn, D. Blaschke, and H. H. Wolter, Phys. Rev. C **81**, 015803 (2010); M. Hempel and J. Schaffner-Bielich, Nucl. Phys. **A837**, 210 (2010).

[13] A. W. Steiner, M. Hempel, and T. Fischer, Astrophys. J. **774**, 17 (2013).
[14] A. W. Steiner, J. M. Lattimer, and E. F. Brown, Astrophys. J. Lett. **765**, L5 (2013).
[15] T. Fischer, M. Hempel, I. Sagert, Y. Suwa, and J. Schaffner-Bielich, Eur. Phys. J. A **50**, 46 (2014).
[16] S. Bernuzzi, A. Nagar, S. Balmelli, T. Dietrich, and M. Ujevic, Phys. Rev. Lett. **112**, 201101 (2014).
[17] E. Gourgoulhon, P. Grandclement, K. Taniguchi, J.-A. Marck, and S. Bonazzola, Phys. Rev. D **63**, 064029 (2001).
[18] S. Bernuzzi and D. Hilditch, Phys. Rev. D **81**, 084003 (2010).
[19] F. Galeazzi, W. Kastaun, L. Rezzolla, and J. A. Font, Phys. Rev. D **88**, 064009 (2013); D. Radice, F. Galeazzi, J. Lippuner, L. F. Roberts, C. D. Ott, and L. Rezzolla (to be published).
[20] F. Löffler *et al.*, Classical Quantum Gravity **29**, 115001 (2012).
[21] D. Radice and L. Rezzolla, Astron. Astrophys. **547**, A26 (2012); D. Radice, L. Rezzolla, and F. Galeazzi, Mon. Not. R. Astron. Soc. **437**, L46 (2014); Classical Quantum Gravity **31**, 075012 (2014).
[22] S. Bernuzzi, T. Dietrich, and A. Nagar, Phys. Rev. Lett. **115**, 091101 (2015).
[23] K. Kiuchi, P. Cerdá-Durán, K. Kyutoku, Y. Sekiguchi, and M. Shibata, Phys. Rev. D **92**, 124034 (2015).
[24] S. Richers *et al.* (to be published).
[25] S. Bernuzzi, A. Nagar, M. Thierfelder, and B. Brugmann, Phys. Rev. D **86**, 044030 (2012).
[26] T. Damour, A. Nagar, D. Pollney, and C. Reisswig, Phys. Rev. Lett. **108**, 131101 (2012).
[27] M. Campanelli, C. O. Lousto, and Y. Zlochower, Phys. Rev. D **74**, 084023 (2006).
[28] D. A. Hemberger, G. Lovelace, T. J. Loredo, L. E. Kidder, M. A. Scheel, B. Szilágyi, N. W. Taylor, and S. A. Teukolsky, Phys. Rev. D **88**, 064014 (2013).
[29] U. Sperhake, E. Berti, V. Cardoso, and F. Pretorius, Phys. Rev. Lett. **111**, 041101 (2013).
[30] J. A. Clark, A. Bauswein, N. Stergioulas, and D. Shoemaker, Classical Quantum Gravity **33**, 085003 (2016).
[31] K. Kiuchi (private communication).
[32] P. Mösta, C. D. Ott, D. Radice, L. F. Roberts, E. Schnetter, and R. Haas, Nature (London) **528**, 376 (2015).
[33] I. Zalamea and A. M. Beloborodov, Mon. Not. R. Astron. Soc. **410**, 2302 (2011).
[34] E. Nakar, Phys. Rep. **442**, 166 (2007).